INORGANIC CHEMISTRY FRONTIERS

RESEARCH ARTICLE

View Article Online
View Journal | View Issue

Cite this: *Inorg. Chem. Front.*, 2024, **11**, 3001

Tuning lithium–yttrium chloride local structure through coordination control and mixing during synthesis†

Teerth Brahmbhatt,[a,b] Cheng Li,[c] Mounesha N. Garaga, [d] Wan-Yu Tsai, [a] Steve G. Greenbaum, [d] Jagjit Nanda[e,f] and Robert L. Sacci [a]*

Received 1st March 2024,
Accepted 15th April 2024

DOI: 10.1039/d4qi00559g

rsc.li/frontiers-inorganic

Lithium halide-based solid electrolytes have high Li^+ conductivity and can be synthesized through low-temperature aqueous solution routes. While Li_3InCl_6 can be readily synthesized through dehydration, other analogous materials, such as Li_3YCl_6, cannot. This difference may be due to differences in H_2O coordination strength, which leads to partial hydrolysis to form YOCl. In this work, we followed and compared Li_3YCl_6 synthesis using three different methods using *in situ* neutron diffraction. The data revealed that forming an ammonium halide complex intermediate is essential in synthesizing Li_3YCl_6 from an aqueous solution. In carefully examining the Li_3YCl_6 products, we found that changes in local structure follow on to drive significant differences in ionic transport and Li^+ diffusivity as determined through diffusion NMR measurements. These changes were ascribed to the change in the correlative transport of Li^+. This work provides insight into the reaction mechanisms involved in synthesizing halide solid electrolytes and highlights the importance of considering their synthetic and processing conditions to optimize their performance in all-solid-state batteries.

1. Introduction

The demand for denser, safer, and more portable energy storage has led to significant interest in all-solid-state batteries (ASSBs) and solid electrolytes.[1] Solid Electrolytes enable the replacement of conventional flammable organic liquid electrolytes[2] and span many material classes including polymers,[3] oxides,[4] sulfides,[5] hydrides,[6] and more recently, halides.[7] Halide solid electrolytes have shown promise due to their high ionic conductivity, high voltage cathode compatibility, and adaptability in synthesis and processing routes.[8] Compositions such as Li_3InCl_6 have garnered interest due to their compatibility with aqueous and organic solvent-based synthesis.[9,10] Direct synthesis of other A_3MX_6 (A = Li, M = Sc, Y, Ho, Yb, Er, *etc.*, X = F, Cl, Br, I) compositions in water or other solvents is limited due to the hydrolysis of $MCl_3{\cdot}nH_2O$ intermediates upon heating. This decomposition route leads to the formation of MOCl and LiCl impurities. However, recent reports have shown that it is possible to synthesize these other compositions in water using ammonium halide coordination reagents.[11,12]

This report provides a detailed examination of the formation pathway for Li_3YCl_6 and establishes synthesis-structure property correlations to guide the optimization of halide solid electrolyte-based ASSBs. Large-scale synthesis and optimization of battery materials is not trivial[13,14] and often requires process monitoring. A key enabler of large-scale chemical production is an intimate understanding of the reaction mechanism during synthesis.[15] In addition, many solid electrolyte properties are greatly influenced by the chosen synthesis route.[16] The formation mechanism of halide solid electrolytes through these novel solvent-based routes is poorly understood. Previous work suggested that the addition of ammonium halides resulted in the formation of a complex halide intermediate of the form $(NH_4)_3MX_6$, eqn (1).[17,18] This intermediate, shown in Fig. 1, is suspected to provide an alternative

[a]*Chemical Sciences Division, Oak Ridge National Laboratory, Oak Ridge, TN 37830, USA. E-mail: saccirl@ornl.gov*
[b]*Bredesen Center for Interdisciplinary Research and Education, University of Tennessee, Knoxville, TN 37996, USA*
[c]*Neutron Scattering Division, Oak Ridge National Laboratory, Oak Ridge, TN 37830, USA*
[d]*Department of Physics and Astronomy, Hunter College, City University of New York, New York, NY 10065, USA*
[e]*Applied Energy Division, SLAC National Laboratory, Menlo Park, CA 94025, USA*
[f]*Materials Science and Engineering, Stanford University, Stanford, CA 94035, USA*

†Electronic supplementary information (ESI) available: Showing powder diffraction of phase transitions and refinements in more detail. See DOI: https://doi.org/10.1039/d4qi00559g

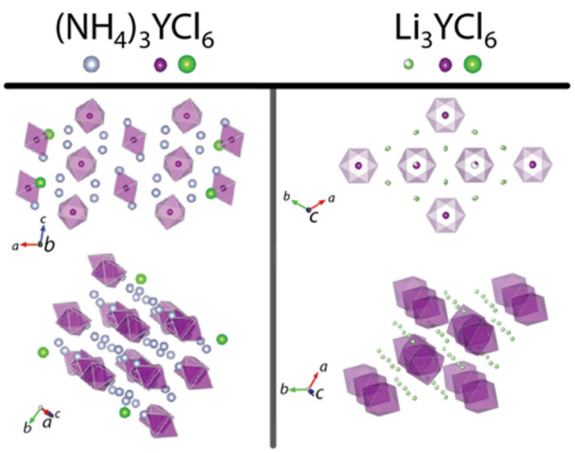

Fig. 1 Representative crystal structures of the $(NH_4)_3YCl_6$ and anhydrous Li_3YCl_6 phases. Octahedrals represent YCl_6^{3-} polyanions.

reaction route away from the oxyhalide formation side reaction (eqn (2)) during the dehydration and the subsequent annealing steps at 350–550 °C.

$$YCl_3 \cdot nH_2O + 3\,NH_4Cl \xrightarrow{-nH_2O} (NH_4)_3YCl_6 \quad (1)$$

$$YCl_3 \cdot nH_2O \xrightarrow{\Delta} YOCl + (n-1)H_2O + 2HCl \quad (2)$$

We utilized *in situ* neutron powder diffraction (NPD) to track the formation of Li_3YCl_6 (LYC) across multiple synthesis routes. NPD is well suited for probing reactions at relevant mass scales due to its high penetrative power and sensitivity to Li.[19,20] In addition, neutrons are far more sensitive to protons and deuterons groups within NH_4Cl and complex halide intermediates than X-ray diffraction. Deuterated precursors (D_2O and ND_4Cl) were used for NPD experiments to minimize the incoherent scattering background of protons. We confirmed the formation of $(ND_4)_3YCl_6$ during the aqueous synthesis of LYC and its decomposition. We show that dehydration of the complex before reaching high temperatures is critical even in the wet chemical synthesis route to avoid the formation of LiCl and YOCl impurities. We observe in multiple reaction mechanisms that the LYC formation and then melting at higher temperatures is crucial to driving proper mixing of precursors and intermediates, agreeing with a previous report by Asano *et al.* where LYC was thermally stable up to 450 °C.[21] To our knowledge, this is the first instance of providing structural characterization after melting the solid electrolyte phase using *in situ* diffraction techniques.[22] Melting of the LYC phase could play an essential role in separator fabrication through melt infiltration or casting methods.[23] We characterize the influence of the LYC synthesis route on the ionic and electronic conductivity and observe the significant role of grain boundaries in the total ionic conductivity of LYC solid electrolytes that undergo annealing.

2. Experimental

2.1 Synthesis

The aqueous ammonium coordinated (AC) and ammonium free (AF) synthesis of LYC was prepared by weighing out 34 mol% excess of anhydrous YCl_3 (Sigma Aldrich 99.99%, 451363), stoichiometric amounts of LiCl (Sigma Aldrich 99%, 793620) and NH_4Cl (Sigma Aldrich 99.5%, A4514) in a 1 : 3 : 3 molar ratio in a glovebox (1 : 3 : 0 for AF synthesis). The mixture was then transferred to a round bottom flask and dissolved in DI water, sonicated for 15 minutes, and excess water was evaporated *via* rotovap. The sample was then dried overnight at 150 °C under vacuum to remove excess water. The white powder was ground in an agate mortar and pestle, pelletized, placed in an alumina combustion boat, and annealed at 500 °C (heating rate 5 °C min^{-1}) for 5 h under argon flow (30 mL min^{-1}) in a glovebox.

The mechanochemical (MC) synthesis of Li_3YCl_6 was conducted in a Fritsch Pulvirisette 7 planetary ball mill. Here, the LiCl and anhydrous YCl_3 were loaded into zirconia milling jars (45 mL volume) with Y-stabilized zirconia milling media (5 mm diameter) inside a glovebox. The media-to-powder ratio was 30 : 1. The mixture was milled at 510 rpm for 48 cycles with 15 min of milling and a 15 min pausing step to allow the sample to cool; after the initial 48 cycles, the jar was taken into a glovebox, and the sample was scraped off the walls of the jar to prevent the formation of hot zones during milling, this was followed by another 48 cycles under the same conditions. The milled powder was pelletized and annealed at equivalent conditions to the AC and AF samples. For clarity, this sample is referred to as the mechanochemical annealed (MCA) sample, and the unannealed sample is referred to as the MC sample.

2.2 Characterization

Ex situ NPD patterns were collected on POWGEN (BL-11A) at 1.5 Å wavelength. The samples were loaded into vanadium cans under an argon atmosphere in a glovebox and sealed with copper gaskets and aluminum lids. The patterns were measured at 300 K. The samples were absorption corrected after data collection. Rietveld refinements against the neutron diffraction data were performed using GSAS II.[24] The following parameters were refined: (1) background using a Chebyshev polynomial with 10 coefficients, (2) scale factor, (3) sample-induced peak broadening, (4) lattice parameters, (5) atomic positions, (6) isotropic thermal displacement parameters, and (7) occupancies.

The loss of ammonium salt was confirmed using infrared spectroscopy using an Agilent Cary 650 spectrometer equipped with an attenuated total reflection accessory (Specac Ltd). Before measurement, the samples were protected from moisture by sealing them in the diamond crystal holder in a glovebox.

2.2.1 Impedance spectroscopy. The solid electrolyte samples were pelletized at 5.9 t cm^{-2} for 1 min in a 12.7 mm die set with carbon-coated aluminum foil on either side to be

used as blocking electrodes for the ionic conductivity measurements. The measurements were performed by electrochemical impedance spectroscopy (EIS) at OCV, applying an excitation amplitude of 10 mV in a frequency range between 7 MHz and 100 mHz with 6 points per decade using a VSP potentiostat (Biologic).

2.2.2 DSC and TGA. TA instruments TGA Q500 and DSC Q100 were used to measure thermogravimetry and differential scanning calorimetry (TGA and DSC), respectively. The samples were loaded into aluminum pans and heated to 500 °C at a heating rate of 5 °C min^{-1} under a nitrogen flow of 50 mL min^{-1}.

2.2.3 *In situ* neutron diffraction. To follow the product distribution of a larger scale reaction, large pellets (~3–5 grams) of the post-vacuum dried AC, AF, and MC samples were loaded into separate quartz baskets along with quartz wool. The basket was placed into the AGES gas flow system at POWGEN (BL-11A) diffractometer at the Spallation Neutron Source (SNS) at Oak Ridge National Laboratory.[25,26] An initial room temperature scan was taken and then ramped to 500 °C at a rate of 5 °C min^{-1} under flowing Ar, with 1 h holds at 100, 200, 300, 400, and 500 °C for ND data collection. Samples were cooled and monitored in event mode to enable the re-binning of data after the experiment. ND data were collected at a 1.5 Å center wavelength that covered a *d*-space range of 0.7 to 8 Å. Refinements of all the neutron-diffraction data were conducted using the Rietveld method in GSAS-II.[24] For the neutron-diffraction spectra, the background was fitted using log-interpolated polynomials.

2.2.4 NMR spectroscopy. 1D ^{7}Li static and diffusion NMR measurements were performed on a 300 MHz NMR spectrometer equipped with a DOTY Z-spec PFG NMR probe. The stimulated echo pulse sequence was used to collect the ^{7}Li signal by varying the gradient strength up to the gradient probe with a maximum gradient of 900 G cm^{-1}. The diffusion coefficients were measured with varying temperatures (from 25 °C to 88 °C) and gradient pulse separation (Δ) from 40 ms to 150 ms with gradient pulse length (δ) of 4 ms. The diffusion coefficients were calculated by using the Stejkal–Tanner equation.[27] 1D ^{7}Li static NMR spectra (single pulse experiment with 90° pulse length of 12.6 μs) were collected with 32 scans and 10 s recycling delay and fitted using DMFIT software.[28] ^{7}Li chemical shifts were externally referenced to 1 M LiTFSI solution.

3. Results and discussion

3.1 Synthesis and phase evolution

Summary plots of *in situ* neutron diffraction measurements are presented in Fig. 2, along with phase evolution and thermal analyses. We compared three reaction routes for LYC production at relatively large scales (3–5 grams): ammonium coordinated (AC), ammonium free (AF), and dry mechanochemical (MC). This sample size aligns with a typical laboratory-scale synthesis procedure. For the two aqueous routes, the precursors (LiCl and YCl_3, with and without ammonium chloride) were dissolved in water and dried in a vacuum at 80 °C before measurement. Note that the deuteron will contribute to coherent scattering, making it possible to observe the formation of complex intermediates during the phase evolution. The reactions were conducted by heating the dried precursors under flowing Ar with a temperature ramp rate set to 5 °C min^{-1} and 1 hour holds at 100, 200, 300, 400, and 500 °C before cooling to room temperature (~30 °C).

After comparing the three ND contour plots, the first observation reveals that the AC route (Fig. 2a) is more complex than the others. At 50 °C, YCl_3 and ND_4Cl precursors are present (identified by peaks at 2.76 and 1.58 Å, respectively), and the diffraction intensities begin to fade at 100 °C (Fig. 2a). We also initially observe both YCl_3 and $YCl_3{\cdot}6H_2O$ (peaks at 2.74 and 3.91 Å respectively), as well as small amounts of ND_4Cl and LiCl (1.93 and 2.96 Å respectively). Rietveld refinement of the patterns within the contour plot quantifies the phase evolution (Fig. 2b). As the guidelines point out, these precursors are consumed and form the $(ND_4)_3YCl_6$ complex intermediate, AYC, at 100 °C (identified by the peak at 3.83 Å). The AYC complex assumes a *C*2/*c* structure of the form Cs_3BiCl_6, where YCl_6^{3-} octahedrals are indeed formed and stabilized.[29] Unlike the final product, trigonal LYC ($P\bar{3}m1$), the cations are not well ordered into rows, as shown in Fig. 1. This reaction is accompanied by an intermediate phase(s), which we call LYC-I. We note here that this intermediate is only seen during the AC route. The formation of AYC is seen in the thermal analysis (Fig. 2b), which displays an endothermic peak at 100 °C (Peak 1) and significant weight loss corresponding to D_2O loss. The AYC complex is not long-lived, being consumed at 200 °C and giving way to more intense LYC-I peaks and YCl_3 formation (Fig. 2a). DSC shows an endothermic process at 175 °C (Peak 2) that appears to be a convolution of the AYC decomposition and LYC-I formation. Between 200 and 500 °C, the phase fraction of LYC-I increases and YCl_3 decreases, ending with LYC-I melting, also congruent with an endothermic feature at 475 °C (Peak 4). Within this range, we also observed an endothermic process with significant mass loss between 330 and 375 °C (Peak 3), which correlates with ND_4Cl decomposition.[30] Given that LYC has known polymorphs and no additional phase was observed in the reaction, we believe LYC-I to be a metastable polymorph.

Ex situ infrared spectroscopy in Fig. S4† confirms the presence of H_2O with NH_4^+ cations with strong vibrations at 3100–3200 cm^{-1} (N–H stretching) and 1420 cm^{-1} (N–H scissoring). These bands are absent after annealing at 350 °C and the O–H bands are absent after annealing at 500 °C. The resulting LYC phase that crystallized from all *in situ* melts was the target trigonal LYC phase ($P\bar{3}m1$). We note that while the YCl_3 impurity appears significant in the AC sample, it is likely the result of the LYC melt dripping through the quartz basket's porous bottom. The *ex situ* samples do not show this impurity in similarly large phase fractions, as discussed later.

The AF sample contour plot (Fig. 2c) begins with LiCl and $YCl_3{\cdot}6D_2O$ phases being present with no anhydrous YCl_3

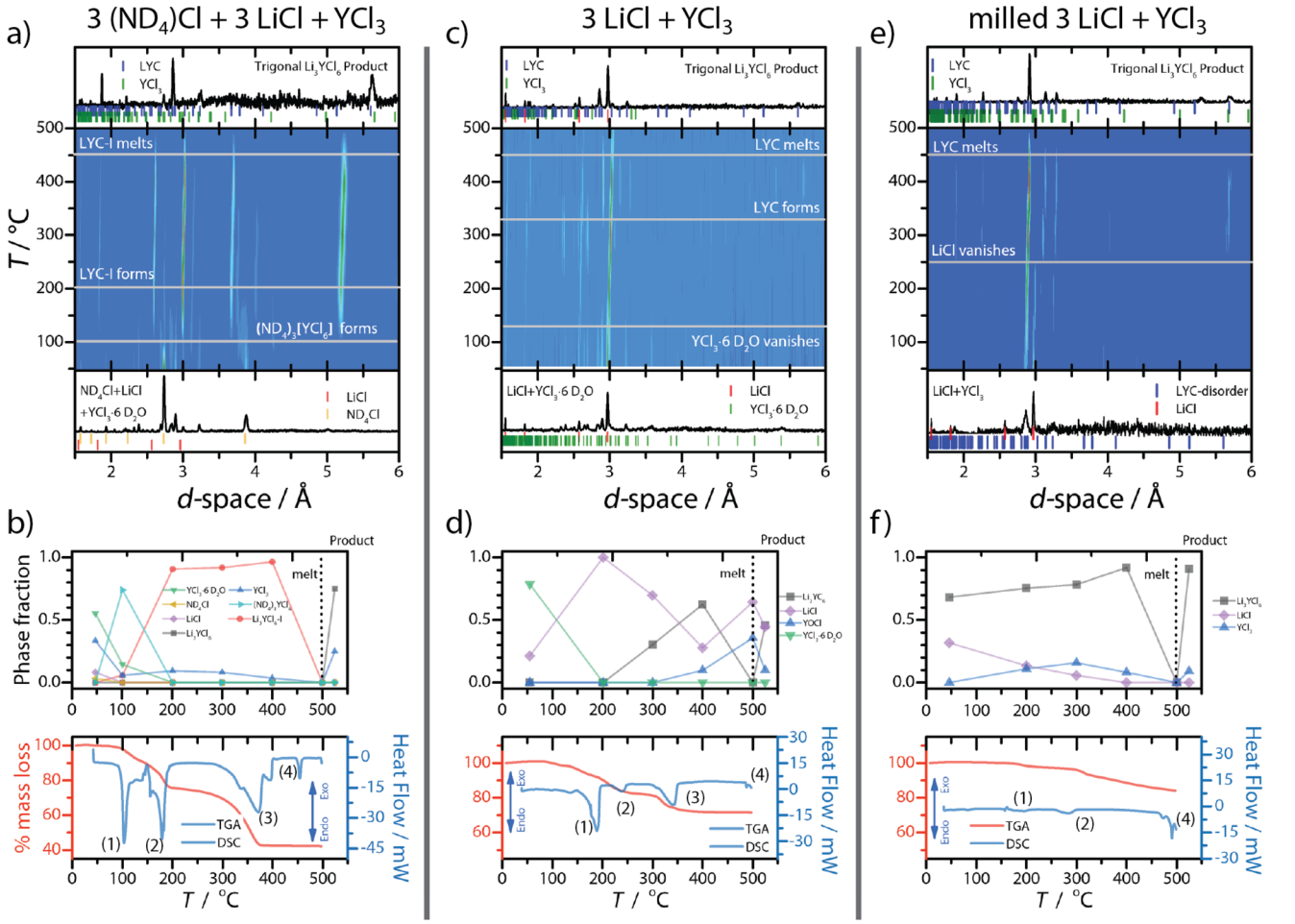

Fig. 2 Visualization of the synthesis pathways using *in situ* neutron diffraction of the AC (a), AF (c), and MC (e), along with their respective phase evolutions with thermal analysis spectra from TGA and DSC (b, d, and f). The contour plots are during heating from 47 to 500 °C only. The initial NPD pattern is the precursors after dissolution and vacuum drying (or mixing) prior to ramping, and the final NPD pattern is the RT product obtained after cooling. Endothermic peaks are numbered for textual clarity (see Fig. S1–3† for high-resolution images).

phase detected (Fig. 2d). The DSC shows no feature at 100 °C associated with intermediate complexes (Fig. 2d); however, during heating to 175 °C the DSC curve shows a large endothermic process alongside substantial mass loss (Peak 1). These results correlate with YCl_3 hydrate consumption and LYC formation in Fig. 2d. The LYC formed here is the targeted trigonal phase and is associated with the second more minor endothermic process in the DSC (230 °C, Peak 2 in DSC). The consumption of the YCl_3 hydrate also results in the formation of the YOCl impurity phase that is formed around 350 °C (Peak 3).[31] This fact demonstrates that the synthesis routes result in differing intermediate phases and reaction kinetics and may allow for trapping novel metastable phases. LYC continues to increase until 500 °C when it melts, leaving insoluble YOCl and LiCl behind. DSC shows LYC melting as a smaller endothermic peak at 475 °C (Peak 4) commensurate with this route's less efficient LYC formation. After cooling, LYC reforms while YOCl and LiCl impurities remain, allowing us to conclude that ammonium chloride is required to protect the YCl_3 precursor from hydrolysis during heating.

Fig. 2e and f show MC reaction route evolution starting with planetary milled LiCl and YCl_3 for 24 h. This reaction proceeds through the most direct route, with LYC being already formed with unreacted LiCl at 68 and 32 wt%, respectively (Fig. 2f). While YCl_3 was not initially detected, we suspect it was present as an amorphous phase, given its immediate appearance with heating. During the temperature ramp, the LiCl phase decreases, and after 175 °C, an endothermic process (Peak 1) is observed and the YCl_3 phase decreases. The latter effect correlated to the small exothermic peak ~275 °C (Peak 2) in Fig. 2f. Again, LYC melts at 475 °C (Peak 3 in the DSC) with residual YCl_3 being present (9 wt%) after cooldown. The LYC phase observed throughout this route was trigonal; however, it started from a nanocrystalline subproduct that has a significant amount of Y2–Y3 site disorder in line with previous reports.[32,33]

We followed the formation of $(ND_4)_3YCl_6$ (AYC) by mixing ND_4Cl and YCl_3 in D_2O using *in situ* NPD (Fig. 3). While solving the crystal structure is outside the scope of this report, we highlight a few findings. The temperature-dependent stack

plot in Fig. 3a shows the initial sample containing anhydrous YCl_3 and ND_4Cl (peaks at 2.76 and 3.94 Å, respectively). As the temperature reaches 100 °C, the ND_4Cl peaks vanish, and the AYC peaks form, which are stable up to 250 °C. The thermal analysis shows residual dehydration and AYC formation are likely convoluted between Peaks 1 and 2 in the DSC. During the AC reaction, AYC was observed during the dehydration, and the peaks vanished as the temperature reached 175 °C (Fig. 2b). This suggests that the reaction to form LYC from AYC through the replacement of ammonia with Li^+ is thermodynamically and kinetically favorable.

This conclusion is reinforced by the fact that Meyer *et al.* proposed a decomposition of $(ND_4)_3[YCl_6]$ back into YCl_3 and NH_4Cl at around 425 °C, which we do not see evidence for in the AC route.[34] We also do not observe the presence of large amounts of LiCl during the AC phase evolution prior to forming Li_3YCl_6, which could signal the existence of a distinct $(NH_4)_3[YCl_6]{\cdot}3LiCl$ composite structure.[11] We note that when comparing the thermal analysis of all the aqueous processes (Fig. 2b, d and f), an approximate weight loss of 30% from room temperature to 200 °C is seen, corresponding to D_2O being removed from the structure. Ammonium chloride allows water to be removed from $YCl_3{\cdot}6H_2O$ without hydrolysis to YOCl at lower temperatures, presumably by shifting the structure from coordination with water to a hexahedral coordination with Cl^-. The last two endothermic peaks (3 and 4) in Fig. 3b do not seem to directly correlate to any observed changes in the *in situ* NPD data. Some possible explanations for this can be gleaned from a similar process observed in the other samples. For the MCA sample, we observe a similar small endothermic peak coinciding with the crystallization of YCl_3 (Peak 1), which could coincide with the YCl_3 observed in the 150 and 250 °C NPD data. Previous work observed a phase transition of NH_4Cl from an α to a β high-temperature phase at 180 °C; however, we do not see the characteristic strong reflection for this phase in the NPD data (the expected peak at 3.298 Å is absent).[34] The final small endothermic process at ~250 °C (Peak 4 in Fig. 3b) could be the consumption of residual YCl_3 as observed in the AF reaction route. Lastly, YOCl formation is not observed in the NPD because the sample stayed below the crystallization temperature (~330 °C).

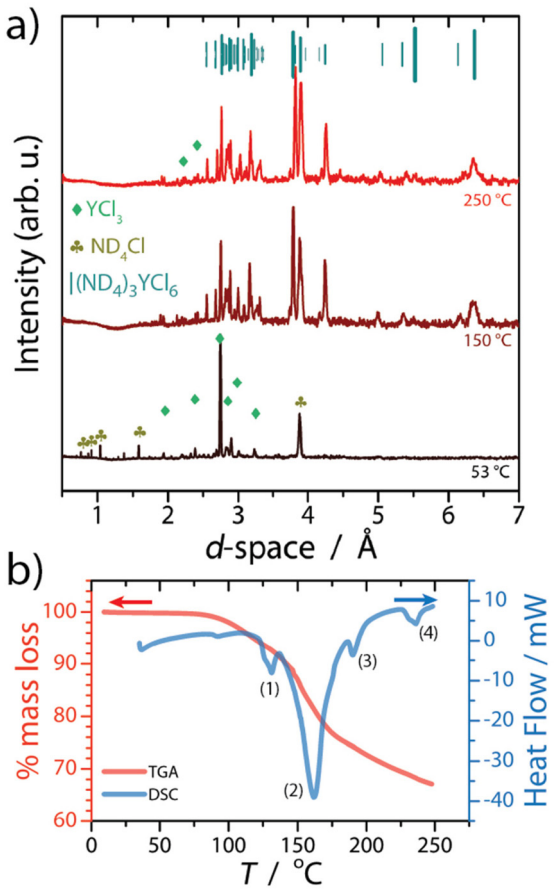

Fig. 3 (a) *in situ* NPD data showing AYC formation heating from ~45 to 250 °C from a dehydrated ND_4Cl + YCl_3 mixture and (b) TGA/DSC of the same precursor. Diffraction tick marks were obtained by phase identification match to Cs_3BiCl_6. Endothermic peaks are labeled for textual clarity.

3.2 Synthesis–structure–property correlation

Recent literature reviews have established the significant relationship between the synthesis route and solid electrolyte properties ranging from the room temperature ionic conductivity to the electrochemical stability window.[16,35] Here, we summarize observations related to atomic structure from ND (lattice parameters), particle morphology, and bulk and grain boundary conductivity. In Fig. 4 we display the Rietveld refinement results for NPD data collected on each of the three products within sealed vanadium cans at room temperature. We note here that the samples always have approximately 5% chloride impurity, whether it was YCl_3 or LiCl. In this study, the impurity was stochastic; however, we didn't apply significant effort in resolving the causal relationship other than annealing drives YCl_3 impurity formation. When comparing the lattice parameters of the MC and MCA samples obtained from NPD, we find that upon annealing, the lattice volume contracts from 662.13 to 659.02 ± 0.02 $Å^3$, and the lattice parameters a and c contract from 11.235 to 11.220 ± 0.001 Å and 6.0573 to 6.0493 ± 0.0006 Å, respectively. The AC product has a similar lattice volume to the MCA sample, 660 $Å^3$. It is possible for the differences in lattice parameters to be driven by Y2–Y3 site disorder, where zero site disorder would correspond to 100% occupation of the Y2 site.[21,33] Upon milling, the MC sample starts with 39% site disorder, and after annealing, this is reduced to 22% site disorder for the MCA sample. This trend of decreasing site disorder as a function of annealing agrees with previous reports.[33]

The degree of disorder can be qualitatively evaluated through ^7Li static NMR. As shown in Fig. 6, the MC sample exhibits two distinct features: a narrow and a broad ^7Li peak. The narrow Gaussian peak itself is a superposition of a quadrupole central transition and a partially narrowed response, which is attributed to Li^+ ions undergoing rapid hopping. At the same time, the latter broad satellite quadrupolar feature

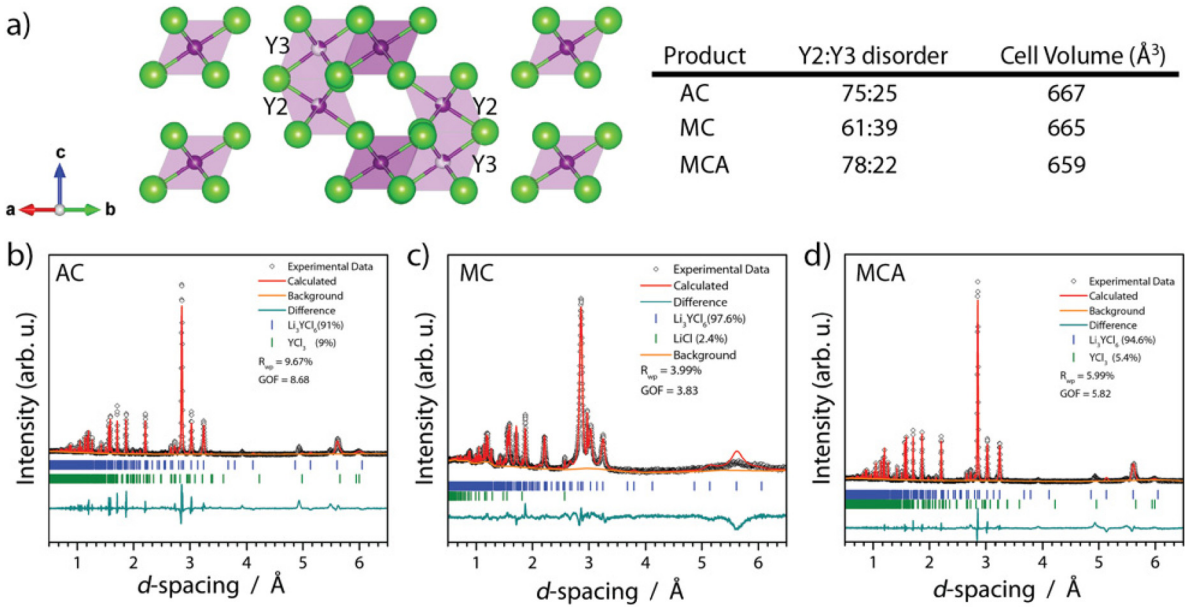

Fig. 4 (a) Refined crystal structure of tetragonal LYC product highlighting the Y2 and Y3 site disorder along with Rietveld refinement of the (b) LYC-AC (c) LYC-MC (d) LYC-MCA products' measured ND data. See Fig. S5–7† for high-resolution images.

corresponds to those occupying crystallographic inequivalent sites.[36] The disorder in the latter is featured by distribution in quadrupolar parameters, resulting in a rounded line shape without well-defined divergences. These narrow and broad peaks converge at elevated temperatures due to rapid Li^+ motion (see Fig. S8†).

In the annealed MCA sample, two distinct ^7Li features have been identified. The peak associated with Li^+ ions situated in inequivalent crystallographic sites exhibits a well-defined quadrupole powder pattern, consistent with the diffraction result that annealing induces ordering in the Li^+ sublattice. On the contrary, the static spectrum of the solution-synthesized AC product reveals three distinct ^7Li features. A single narrow peak is ascribed to the fast-moving Li^+ ions, while two well-defined quadrupolar features are associated with Li^+ ions sited in different inequivalent crystallographic sites. This highlights the more heterogeneous structure of sample AC compared to the MCA sample. In both samples, the quadrupolar features narrow with temperature, which can be attributed to increased Li^+ motion. The representative deconvolution of static spectra is shown in ESI Fig. S9.†

We used electrochemical impedance spectroscopy (EIS) to investigate the impact of the synthesis route on the ionic conductivity and activation energy. The activation energy was obtained by the Arrhenius relationship for solid-state ionic transport in eqn (3),

$$\sigma_{\text{ionic}} T = \sigma_0 \exp\left(-\frac{E_a}{k_B T}\right) \quad (3)$$

where σ_0, k_B, and T are the temperature-independent Arrhenius prefactor, the Boltzmann constant, and the absolute temperature, respectively. σ_0 represents the frequency of lithium hopping events at a standard carrier concentration within the solid ionic conductor.[37,38] Fig. 5a shows representative Nyquist plots showing low ionic resistance and the presence of grain boundaries. For the LYC AC sample, the room temperature lattice ionic conductivity is 0.57 ± 0.05 mS cm^{-1}, while the grain boundary is 0.043 mS cm^{-1}, more than an order of magnitude lower. For the LYC MCA sample, we see a much smaller difference in the two processes, 0.42 ± 0.03 mS cm^{-1} for the lattice *vs.* 0.21 ± 0.01 mS cm^{-1} for the grain boundary. For the MC product, the grains are neglectable, showing 0.47 ± 0.01 mS cm^{-1} for lattice conductivity. Fig. 5b compares the Arrhenius behaviour for the total conductivity of the LYC products, showing that the products have similar values conductivity activation energies of ~0.35 ± 0.01 eV. However, deconvoluting the bulk and grain boundary shows that the activation energy for the lattice conductivity for AC, MC, and MCA are 0.22, 0.15, and 0.17 eV, respectively. This result suggests that the Y distribution between the Y2–Y3 sites strongly influences ionic conduction. The change (a 13% increase in the activation energy) is likely due to the 17% reduction in site disorder observed in the NPD data. This observation is in line with previous reports regarding the effect of annealing time on the mechanochemically synthesized Li_3YCl_6, where it was observed that the conductivity decreased as the milled sample was annealed for more extended periods of time ranging from 1 minute to 1 hour.[33] That said, we also observed an increase of 25% in the grain boundary activation energy, which increased from 0.28 to 0.39 eV between the MC-derived product and the AF product. This shows that microstructure is equally important in determining the ionic transport properties of LYC and must be optimized during synthesis or processing.

PFG NMR was utilized to measure Li^+ diffusivity, D_{Li^+}, as functions of temperature and diffusion time (*i.e.*, gradient pulse

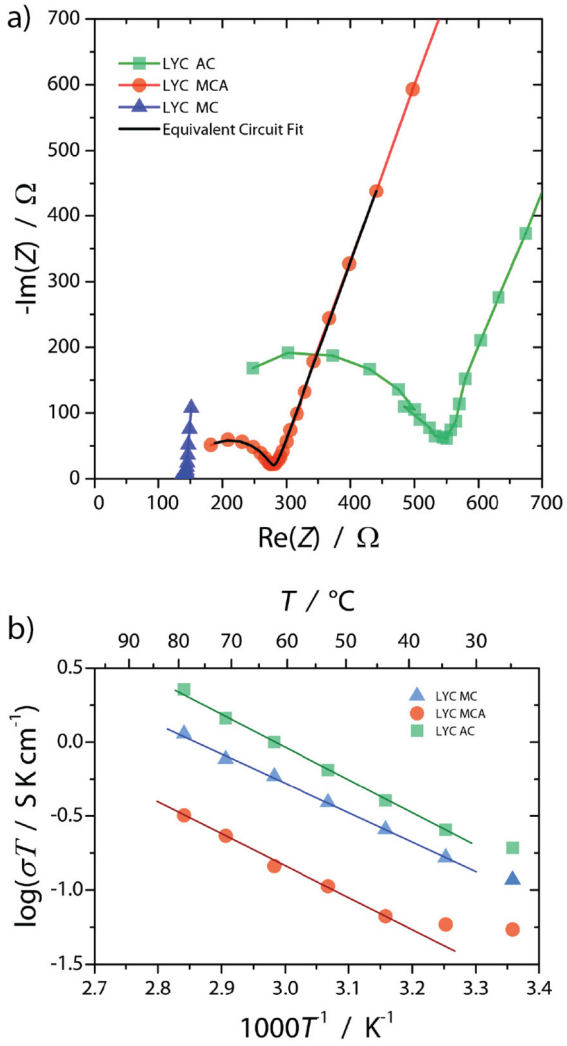

Fig. 5 (a) Representative Nyquist plots of each sample at 35 °C, along with representative fit of the Nyquist plot and equivalent circuit for the LYC MCA sample at 35 °C. (b) Arrhenius plot comparison for the Li_3YCl_6 M, MCA, and AC samples' lattice conductivity.

separation), as displayed in Fig. 7. It is worth noting that, firstly, Li^+ diffusion in MCA is slower compared to AC and MC, which is consistent with conductivity results. Secondly, The D_{Li^+} of AC and MC are found to be comparable. All D_{Li^+} exhibit increase with temperature, demonstrating Arrhenius behavior; E_a = 0.43 eV for AC and MC, and 0.33 eV for MCA. The dependence of D_{Li^+} on Δ shows a decreasing trend for all samples (Fig. 7b). In free isotropic diffusion, D is independent of Δ. The results here indicate that free diffusion is restricted roughly to the length scale of the PFG experiment, given by $\sim(Dt)^{1/2}$, which is on the order of 1 μm and is similar to the average particle size of 800 nm as determined by electron micrographs.

We estimated the correlated migration of the Li^+ ions using the inverse Haven ratio (H_R^{-1}), which is the ratio of the measured conductivity and the theoretically derived value obtained by a tracer diffusion coefficient and the Nernst–Einstein relationship.

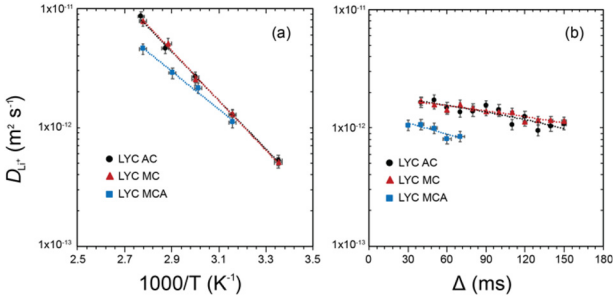

Fig. 7 Diffusion coefficients of Li^+ of AC (black circle), MC (red triangle) and MCA (blue square) measured as a function of (a) temperature from 25 to 88 °C and (b) gradient pulse separation (Δ) from 40 ms to 150 ms.

$$\sigma_{diff} = \frac{ne^2}{k_B T} D_{Li^+} \quad (4)$$

where n is the concentration of the mobile ion. We assumed Li^+ motion is from the more mobile one of the two lithium sites. When H_R^{-1} is greater than unity, correlated charge motion is present. For the sake of comparison, we hold n constant for each sample at 6.8×10^{-3} Li^+ $Å^{-3}$; thus, the values in Table 1 have convolutions of correlated motion and mobile Li^+ concentration. The table shows that the solution and mechanochemical-synthesized products have higher correlated

Table 1 Inverse Haven ratio (H_R^{-1}) of Li_3YCl_6 products

Product	H_R^{-1} at 25 °C	H_R^{-1} at 70 °C
AC	2.69	2.55
MC	1.80	1.47
MCA	0.35	0.62

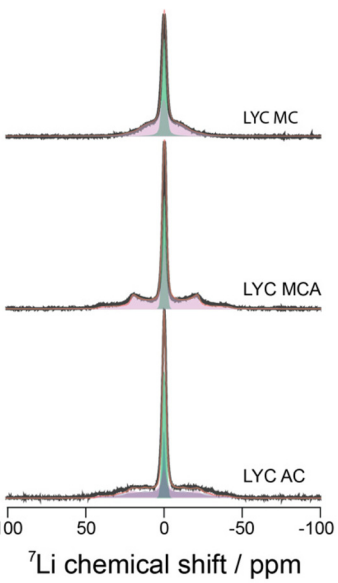

Fig. 6 ^7Li static NMR spectra of MC, MCA, and AC samples and the deconvolution fits.

migration than the annealed sample. These results are similar in value to those obtained for doped and undoped Li_3ScCl_6.[39] H_R^{-1} decreases with temperature, suggesting that more Li^+-ions become mobile or more correlated jumps occur during self-diffusion. We note that H_R^{-1} is significantly suppressed for the MCA sample, being below unity, suggesting that grain boundary influences affect the conductivity measurement. That said, given the contraction of the lattice due to annealing and the well-defined quadrupole satellite peaks in the static ^7Li NMR (Fig. 6), a significant portion of the Li^+ is in well-defined sites, suggesting that the mobile Li^+ concentration is less than the other two samples. These results highlight the correlations between the synthesis procedure and the microstructure of the product.

4. Conclusions

Our work compares the reaction mechanism across multiple synthetic routes, showing that LYC formation differs in terms of intermediate phases and kinetics. Aqueous ammonium coordinated routes are a promising strategy for optimizing not only the performance of halide solid electrolytes but also the processing and, eventually, large-scale production. We show the importance of forming complex halide intermediates necessary to synthesize Li_3YCl_6 through aqueous routes. Control of this intermediate is the key to enabling process control for large batch reactor reaction engineering for halide solid electrolytes. The LYC products were also found to differ significantly in their ionic transport. These differences are shown to be driven by changes in local microstructure, which affected the correlated Li^+ transport or the concentration of mobile Li^+. We find annealing of LYC induces grain boundary formation regardless of the synthesis route. For the LYC properties to be optimized for use in either halide-based or bilayer-based ASSBs, careful consideration must be made as to the ideal synthesis route to use for both processing and optimization performance. Potential future directions include optimizing processing parameters to enable microstructures with smaller grain boundary resistance and favorable particle size distributions, as well as exploring novel liquid-phase techniques compatible with higher and lower valence transition metal chlorides such as $ZrCl_2$ and $HfCl_2$.

Conflicts of interest

There are no conflicts to declare.

Acknowledgements

This project was supported by the Vehicle Technologies Office (VTO) under the Office of Energy Efficiency and Renewable Energy (EERE) as part of the Battery Materials Research (BMR) program. The NPD experiments were conducted at the Spallation Neutron Source, and the SEM was conducted at the Center for Nanophase Materials Sciences; both are DOE Office of Science User Facilities operated by the Oak Ridge National Laboratory.

This manuscript has been authored by UT-Battelle, LLC under Contract No. DE-AC05-00OR22725 with the U.S. Department of Energy. The United States Government retains and the publisher, by accepting the article for publication, acknowledges that the United States Government retains a non-exclusive, paid-up, irrevocable, world-wide license to publish or reproduce the published form of this manuscript, or allow others to do so, for United States Government purposes. The Department of Energy will provide public access to these results of federally sponsored research in accordance with the DOE Public Access Plan (https://energy.gov/downloads/doe-public-access-plan).

References

1 J. Janek and W. G. Zeier, A Solid Future for Battery Development, *Nat. Energy*, 2016, **1**(9), 16141, DOI: 10.1038/nenergy.2016.141.

2 J. Wang, R. Chen, L. Yang, M. Zan, P. Chen, Y. Li, W. Li, H. Yu, X. Yu, X. Huang, L. Chen and H. Li, Raising the Intrinsic Safety of Layered Oxide Cathodes by Surface Re–Lithiation with LLZTO Garnet–Type Solid Electrolytes, *Adv. Mater.*, 2022, **34**(19), 2200655, DOI: 10.1002/adma.202200655.

3 L. Yue, J. Ma, J. Zhang, J. Zhao, S. Dong, Z. Liu, G. Cui and L. Chen, All Solid-State Polymer Electrolytes for High-Performance Lithium Ion Batteries, *Energy Storage Mater.*, 2016, **5**, 139–164, DOI: 10.1016/j.ensm.2016.07.003.

4 M. Jia, N. Zhao, H. Huo and X. Guo, Comprehensive Investigation into Garnet Electrolytes Toward Application-Oriented Solid Lithium Batteries, *Electrochem. Energy Rev.*, 2020, **3**(4), 656–689, DOI: 10.1007/s41918-020-00076-1.

5 X. Bai, T. Yu, Z. Ren, S. Gong, R. Yang and C. Zhao, Key Issues and Emerging Trends in Sulfide All Solid State Lithium Battery, *Energy Storage Mater.*, 2022, **51**, 527–549, DOI: 10.1016/j.ensm.2022.07.006.

6 Y. Pang, Y. Liu, J. Yang, S. Zheng and C. Wang, Hydrides for Solid-State Batteries: A Review, *Mater. Today Nano*, 2022, **18**, 100194, DOI: 10.1016/j.mtnano.2022.100194.

7 H. Kwak, S. Wang, J. Park, Y. Liu, K. T. Kim, Y. Choi, Y. Mo and Y. S. Jung, Emerging Halide Superionic Conductors for All-Solid-State Batteries: Design, Synthesis, and Practical Applications, *ACS Energy Lett.*, 2022, **7**(5), 1776–1805, DOI: 10.1021/acsenergylett.2c00438.

8 C. Wang, J. Liang, J. T. Kim and X. Sun, Prospects of Halide-Based All-Solid-State Batteries: From Material Design to Practical Application, *Sci. Adv.*, 2022, **8**(36), eadc9516, DOI: 10.1126/sciadv.adc9516.

9 X. Li, J. Liang, N. Chen, J. Luo, K. R. Adair, C. Wang, M. N. Banis, T. Sham, L. Zhang, S. Zhao, S. Lu, H. Huang, R. Li and X. Sun, Water–Mediated Synthesis of a Superionic

Halide Solid Electrolyte, *Angew. Chem., Int. Ed.*, 2019, **58**(46), 16427–16432, DOI: 10.1002/anie.201909805.

10 X. Luo, D. Cai, X. Wang, X. Xia, C. Gu and J. Tu, A Novel Ethanol-Mediated Synthesis of Superionic Halide Electrolytes for High-Voltage All-Solid-State Lithium–Metal Batteries, *ACS Appl. Mater. Interfaces*, 2022, **14**(26), 29844–29855, DOI: 10.1021/acsami.2c06216.

11 C. Wang, J. Liang, J. Luo, J. Liu, X. Li, F. Zhao, R. Li, H. Huang, S. Zhao, L. Zhang, J. Wang and X. Sun, A Universal Wet-Chemistry Synthesis of Solid-State Halide Electrolytes for All-Solid-State Lithium-Metal Batteries, *Sci. Adv.*, 2021, **7**(37), eabh1896, DOI: 10.1126/sciadv.abh1896.

12 X. Shi, Z. Zeng, H. Zhang, B. Huang, M. Sun, H. H. Wong, Q. Lu, W. Luo, Y. Huang, Y. Du and C. Yan, Gram–Scale Synthesis of Nanosized Li_3HoBr_6 Solid Electrolyte for All–Solid–State Li–Se Battery, *Small Methods*, 2021, **5**(11), 2101002, DOI: 10.1002/smtd.202101002.

13 M. R. Palacin, Battery Materials Design Essentials, *Acc. Mater. Res.*, 2021, **2**(5), 319–326, DOI: 10.1021/accountsmr.1c00026.

14 R. Jain, A. S. Lakhnot, K. Bhimani, S. Sharma, V. Mahajani, R. A. Panchal, M. Kamble, F. Han, C. Wang and N. Koratkar, Nanostructuring versus Microstructuring in Battery Electrodes, *Nat. Rev. Mater.*, 2022, **7**(9), 736–746, DOI: 10.1038/s41578-022-00454-9.

15 V. Sebastian, M. Arruebo and J. Santamaria, Reaction Engineering Strategies for the Production of Inorganic Nanomaterials, *Small*, 2014, **10**(5), 835–853, DOI: 10.1002/smll.201301641.

16 A. Banik, T. Famprikis, M. Ghidiu, S. Ohno, M. A. Kraft and W. G. Zeier, On the Underestimated Influence of Synthetic Conditions in Solid Ionic Conductors, *Chem. Sci.*, 2021, **12**(18), 6238–6263, DOI: 10.1039/D0SC06553F.

17 M. Simon and G. Meyer, The Oxidation of Tantalum with Ammonium Chloride as an Example of a Novel Route to Early Transitional Metal–Nitrogen Cluster Compounds. Synthesis and Crystal Structure of $(NH_4)_6[Ta_5(NH)_4Cl_{17}]$, *J. Chem. Soc., Chem. Commun.*, 1993, (5), 460–461, DOI: 10.1039/C39930000460.

18 G. Meyer, E. Garcia and J. D. Corbett, The Ammonium Chloride Route to Anhydrous Rare Earth Chlorides-The Example of YCl_3, in *Inorganic Syntheses*, ed. H. R. Allcock, John Wiley & Sons, Inc., Hoboken, NJ, USA, 2007, pp. 146–150. DOI: 10.1002/9780470132562.ch35.

19 R. L. Sacci, T. H. Bennett, A. R. Drews, V. Anandan, M. J. Kirkham, L. L. Daemen and J. Nanda, Phase Evolution during Lithium–Indium Halide Superionic Conductor Dehydration, *J. Mater. Chem. A*, 2021, **9**(2), 990–996, DOI: 10.1039/D0TA10012A.

20 R. L. Sacci, R. D. McAuliffe, T. F. Malkowski, N. Kidder, X. C. Chen, A. Huq, M. Kirkham, B. L. Armstrong, L. L. Daemen and G. M. Veith, $La_2Zr_2O_7$ Nanoparticle-Mediated Synthesis of Porous Al-Doped $Li_7La_3Zr_2O_{12}$ Garnet, *Inorg. Chem.*, 2021, **60**(13), 10012–10021, DOI: 10.1021/acs.inorgchem.1c01300.

21 T. Asano, A. Sakai, S. Ouchi, M. Sakaida, A. Miyazaki and S. Hasegawa, Solid Halide Electrolytes with High Lithium-Ion Conductivity for Application in 4 V Class Bulk-Type All-Solid-State Batteries, *Adv. Mater.*, 2018, **30**(44), 1803075, DOI: 10.1002/adma.201803075.

22 Y. Wu, S. Wang, H. Li, L. Chen and F. Wu, Progress in Thermal Stability of all–solid–state–Li–ion–batteries, *InfoMat*, 2021, **3**(8), 827–853, DOI: 10.1002/inf2.12224.

23 Y. Xiao, K. Turcheniuk, A. Narla, A.-Y. Song, X. Ren, A. Magasinski, A. Jain, S. Huang, H. Lee and G. Yushin, Electrolyte Melt Infiltration for Scalable Manufacturing of Inorganic All-Solid-State Lithium-Ion Batteries, *Nat. Mater.*, 2021, **20**(7), 984–990, DOI: 10.1038/s41563-021-00943-2.

24 B. H. Toby and R. B. Von Dreele, *GSAS-II*: The Genesis of a Modern Open-Source All Purpose Crystallography Software Package, *J. Appl. Crystallogr.*, 2013, **46**(2), 544–549, DOI: 10.1107/S0021889813003531.

25 M. Kirkham, L. Heroux, M. Ruiz-Rodriguez and A. Huq, AGES: Automated Gas Environment System for *in Situ* Neutron Powder Diffraction, *Rev. Sci. Instrum.*, 2018, **89**(9), 092904, DOI: 10.1063/1.5031432.

26 A. Huq, M. Kirkham, P. F. Peterson, J. P. Hodges, P. S. Whitfield, K. Page, T. Hűgle, E. B. Iverson, A. Parizzi and G. Rennich, POWGEN: Rebuild of a Third-Generation Powder Diffractometer at the Spallation Neutron Source, *J. Appl. Crystallogr.*, 2019, **52**(5), 1189–1201, DOI: 10.1107/S160057671901121X.

27 E. O. Stejskal and J. E. Tanner, Spin Diffusion Measurements: Spin Echoes in the Presence of a Time-Dependent Field Gradient, *J. Chem. Phys.*, 1965, **42**(1), 288–292.

28 D. Massiot, F. Fayon, M. Capron, I. King, S. Le Calvé, B. Alonso, J.-O. Durand, Z. Gan and G. Hoatson, Modelling One- and Two-Dimensional Solid-State NMR Spectra, *Magn. Reson. Chem.*, 2002, **40**, 70–76, DOI: 10.1002/mrc.984.

29 H. Mattfeld and G. Meyer, Ternäre Halogenide Vom Typ A3MX6. I A3YCl6 (A = K, NH4, Rb, Cs): Synthese, Strukturen, Thermisches Verhalten. Über Einige Analoge Chloride Der Lanthanide, *Z. Anorg. Allg. Chem.*, 1992, **618**(12), 13–17, DOI: 10.1002/zaac.19926180103.

30 G. Yudoyono, N. Ichzan, V. Zharvan, R. Daniyati, H. Santoso, B. Indarto, Y. H. Pramono and M. Zainuri, Darminto. Effect of Calcination Temperature on the Photocatalytic Activity of TiO2 Powders Prepared by Co-Precipitation of TiCl3; Semarang, Indonesia, 2016, p. 020099. DOI: 10.1063/1.4945553.

31 P. K. Todd, M. J. McDermott, C. L. Rom, A. A. Corrao, J. J. Denney, S. S. Dwaraknath, P. G. Khalifah, K. A. Persson and J. R. Neilson, Selectivity in Yttrium Manganese Oxide Synthesis via Local Chemical Potentials in Hyperdimensional Phase Space, *J. Am. Chem. Soc.*, 2021, **143**(37), 15185–15194, DOI: 10.1021/jacs.1c06229.

32 M. Gombotz and H. M. R. Wilkening, Fast Li Ion Dynamics in the Mechanosynthesized Nanostructured Form of the Solid Electrolyte Li_3YBr_6, *ACS Sustainable*

Chem. Eng., 2021, **9**(2), 743–755, DOI: **10.1021/acssuschemeng.0c06694**.

33 R. Schlem, S. Muy, N. Prinz, A. Banik, Y. Shao-Horn, M. Zobel and W. G. Zeier, Mechanochemical Synthesis: A Tool to Tune Cation Site Disorder and Ionic Transport Properties of Li_3MCl_6 (M = Y, Er) Superionic Conductors, *Adv. Energy Mater.*, 2020, **10**(6), 1903719, DOI: **10.1002/aenm.201903719**.

34 G. Meyer and P. Ax, An Analysis of the Ammonium Chloride Route to Anhydrous Rare-Earth Metal Chlorides, *Mater. Res. Bull.*, 1982, **17**(11), 1447–1455, DOI: **10.1016/0025-5408(82)90231-8**.

35 Y. W. Choi, C. M. Araujo and R. Lizárraga, Amorphisation-Induced Electrochemical Stability of Solid-Electrolytes in Li-Metal Batteries: The Case of Li 3 ClO, *J. Power Sources*, 2022, **521**, 230916, DOI: **10.1016/j.jpowsour.2021.230916**.

36 V. Epp, Ö. Gün, H.-J. Deiseroth and M. Wilkening, Long-Range Li+ Dynamics in the Lithium Argyrodite Li7PSe6 as Probed by Rotating-Frame Spin–Lattice Relaxation NMR, *Phys. Chem. Chem. Phys.*, 2013, **15**, 7123–7132, DOI: **10.1039/C3CP44379E**.

37 V. Jagannadham, How Do We Introduce the Arrhenius Pre-Exponential Factor (A) to Graduate Students?, *Creat. Educ.*, 2010, **01**(02), 128–129, DOI: **10.4236/ce.2010.12019**.

38 Y. Gao, N. Li, Y. Wu, W. Yang and S. Bo, Rethinking the Design of Ionic Conductors Using Meyer–Neldel–Conductivity Plot, *Adv. Energy Mater.*, 2021, **11**(13), 2100325, DOI: **10.1002/aenm.202100325**.

39 R. Li, P. Lu, X. Liang, L. Liu, M. Avdeev, Z. Deng, S. Li, K. Xu, J. Feng, R. Si, F. Wu, Z. Zhang and Y.-S. Hu, Superionic Conductivity Invoked by Enhanced Correlation Migration in Lithium Halides Solid Electrolytes, *ACS Energy Lett.*, 2024, **9**, 1043–1052, DOI: **10.1021/acsenergylett.3c02496**.